



## Research Article

## Controlling microstructure and mechanical properties of Ti-V-Cr-Nb-Ta refractory high entropy alloys through heat treatments



Junliang Liu <sup>a,\*</sup>, Robert J. Scales <sup>a</sup>, Bo-Shiuan Li <sup>a,b</sup>, Michael Goode <sup>a</sup>, Bradley A. Young <sup>a</sup>, Jianan Hu <sup>c</sup>, Angus J. Wilkinson <sup>a</sup>, David E.J. Armstrong <sup>a,\*</sup>

<sup>a</sup> Department of Materials, University of Oxford, Oxford OX1 3PH, UK

<sup>b</sup> Department of Mechanical & Electromechanical Engineering, National Sun-Yat Sen University, No. 70 Lien-hai Rd., Kaohsiung, Taiwan

<sup>c</sup> Sente Software Ltd, Surrey Technology Centre, Guildford GU2 7YG, UK

## ARTICLE INFO

## Article history:

Received 18 August 2022

Received in revised form 12 October 2022

Accepted 17 October 2022

Available online 19 October 2022

## Keywords:

Refractory high entropy alloys

Mechanical properties

Microstructure

Nanoindentation

## ABSTRACT

In this study, we have investigated the microstructure and mechanical properties of two refractory high entropy alloys (RHEAs), Ti-V-Cr5-Nb-Ta and Ti-V-Cr-Nb-Ta, in their as-cast and heat-treated conditions. Both alloys show almost single-phase BCC structure, while different size and volume fraction of secondary phases were formed after homogenisation heat treatment. The major secondary phase was indexed as a complex C15 Laves structure with a composition of (Ti, Ta)(V, Cr, Nb)<sub>2</sub>. The nanoindentation mapping indicates C15 Laves phase is very hard and brittle, performing a homogenisation heat treatment leads to an improved hardness in both alloys. The correlations between hardness changes and microstructural evolutions after homogenisation heat treatment are also discussed.

© 2022 The Authors. Published by Elsevier B.V. This is an open access article under the CC BY license (<http://creativecommons.org/licenses/by/4.0/>).

## 1. Introduction

Refractory high entropy alloys (RHEAs) are a recently developed novel class of materials in which no one element dominates, instead, four or more refractory elements are used in near equal proportions [1]. The RHEAs can also contain non-refractory elements such as Al, Cr or Si to decrease alloy density and/or improve mechanical properties or oxidation resistance [1]. By using refractory elements as the principle alloying elements, RHEAs provide the opportunity to develop higher melting temperature materials, and therefore higher application temperatures comparable to or exceeding current high temperature alloys such as Ni-based superalloys [1]. Lee et al. [2] and Tukac et al. [3] compared the compressive yield strength of various RHEA systems and conventional Ni-based superalloys. All the RHEAs reviewed in [3] show very high yield strength (> 900 MPa) at RT and most retain their high strength at temperatures up to 1000 °C. For example, the Cr<sub>10</sub>Mo<sub>25</sub>Ta<sub>25</sub>Ti<sub>15</sub>V<sub>25</sub> alloy has yield strength 1542 MPa at room temperature and 594 MPa at 1000 °C [3]. In contrast, conventional high-temperature Ni-based superalloy Haynes 230 significantly softens above 700 °C, with its compressive yield strength dropping to ~100 MPa at 1000 °C [3]. The strengthening in conventional Ni-based superalloys is mainly controlled by secondary

phase precipitation. Such behaviour of conventional superalloys is quite different from RHEAs in which lattice distortions or the local compositional fluctuations serve as a solid-solution-like strengthening mechanism and play a primary role in strengthening [1]. In addition, RHEAs exhibit attractive properties like superconductivity and radiation resistance [1,4–7].

It is thought the design of RHEAs with controlled amount and size of secondary phase precipitates would be a beneficial direction for the development of new materials [8–10], with the potential for further enhancements in high-temperature strength and radiation damage resistance. Compositional complexity and the large differences in elemental melting temperatures can produce severe micro- and macro-segregation (often in the form of a dendritic structure) in RHEAs prepared from the liquid state [11]. The homogenisation heat treatment after casting is a useful step to reduce micro- and macro-segregation and enhance the homogeneity of properties across the product [12,13]. Depending on the homogenisation conditions and materials' compositions, RHEAs can exhibit a single-phase BCC structure or a BCC matrix with secondary-phase precipitates [1,14,15]. The Laves phases (C14 or C15) are two of the most commonly seen phases in homogenised RHEAs, especially with the presence of Cr [10,16–18]. For instance, a hexagonal Zr<sub>5</sub>Al<sub>3</sub>-type second phase is introduced into the Al-Nb-Ti-Zr HEA through homogenisation treatment, resulting in an increase of the yield strength, ultimate compressive strength, and fracture strain by 70 MPa, 308 MPa and 9.2%, respectively [8]. Homogenised

\* Corresponding authors.

E-mail addresses: [junliang.liu@materials.ox.ac.uk](mailto:junliang.liu@materials.ox.ac.uk) (J. Liu), [david.armstrong@materials.ox.ac.uk](mailto:david.armstrong@materials.ox.ac.uk) (D.E.J. Armstrong).

**Table 1**  
Melting and boiling points of elements [22].

	Ti	V	Nb	Cr	Ta
Melting point (°C)	1668	1910	2477	1907	3017
Boiling point (°C)	3287	3407	4744	2671	5458

$\text{Al}_{0.5}\text{CrNbTi}_2\text{V}_{0.5}$  RHEA with BCC matrix and a second phase consisting of Ti-, Cr- and Nb-enriched C14 Laves phase, exhibits a room temperature yield strength approximately 10% higher than the as-cast alloy [19]. In addition, the presence of at least some precipitates is typically essential for the design of new structural materials in nuclear applications [20], which can provide efficient sinks to radiation defects, suppress radiation-induced swelling, protect grain boundaries, and increase the creep strength [21].

In this work, two RHEAs with different content of Cr, Ti25-V25-Cr5-Nb20-Ta25 and Ti20-V20-Cr20-Nb20-Ta20 (in at%), were fabricated and investigated with respect to their microstructure and mechanical properties evolutions after annealing at various temperatures. Based on the experimental characterisation and phase calculations, homogenisation heat treatment conditions to achieve RHEAs with a uniform distribution of nano-precipitates are proposed. For brevity, for the rest of this paper, Ti-V-Cr5-Nb-Ta and Ti-V-Cr-Nb-Ta are used to represent Ti25-V25-Cr5-Nb20-Ta25 (at%) and Ti20-V20-Cr20-Nb20-Ta20 (at%) respectively.

## 2. Materials

Two alloys were cast using a plasma arc furnace with a tungsten electrode and electromagnetic stirring in an argon atmosphere. The arc melter works in an argon atmosphere, which is used as both a medium for the plasma between two electrodes, and to protect the molten alloy from reactive atmospheric elements. The cast ingot was flipped and remelted multiple times (at least three) to achieve chemical uniformity at the coarsest length scale. High-purity (>99.95%) raw elements in lump form were obtained from Goodfellow (Goodfellow Cambridge Ltd., UK). The elements used have significantly different melting/boiling points, Table 1. For example, the melting point of Ta is  $\sim 400^\circ\text{C}$  higher than the boiling point of Cr. To reduce the vaporisation of volatile elements, the two highest melting point elements, Ta and Nb, were pre-alloyed.

The composition of the two as-cast RHEAs was measured using X-ray fluorescence (XRF) by AMG Superalloys Ltd, shown in Table 2. These results show that the concentrations were close to the intended compositions and there is no obvious loss of volatile elements e.g. Cr. The concentration of interstitial impurities (C, N and O) are low, therefore their evolution and effects on the microstructure and mechanical properties are not the focus of discussion in this paper.

To study the microstructural stability, as-cast alloys were homogenised at  $800^\circ\text{C}$  and  $1200^\circ\text{C}$  respectively for 48 h under vacuum in sealed quartz-glass tubes, and then water quenched within the tube. Samples were then cut into desired shapes using an IsoMet 5000 linear saw with a 15HC diamond blade. After cutting, the samples were ground with abrasive papers from 600 grit down to 4000 grit, and polished using colloidal silica for around 1 hr. A final ion etching step was performed before EBSD analysis using a Gatan PECS II system with argon ions at 8 kV and an incident angle of  $8^\circ$  for 10 mins.

**Table 2**  
The composition of the as-cast RHEAs investigated in at% (with C, N and O in ppm).

Sample	Designed composition	Ti	V	Cr	Nb	Ta	C	N	O
Ti-V-Cr5-Nb-Ta	Ti25-V25-Cr5-Nb20-Ta25	23.6	24.0	4.7	20.6	27.0	79	75	306
Ti-V-Cr-Nb-Ta	Ti20-V20-Cr20-Nb20-Ta20	20.2	19.0	20.2	19.9	20.8	49	124	431

## 3. Experimental methods

In order to evaluate the possible phases present in the two RHEAs, the phase diagrams were computed using JMatPro®. The X-ray diffraction (XRD) crystal structure analysis was performed using a Rigaku MiniFlex 600 X-ray diffractometer with a Cu target and a step size of  $0.01^\circ$ . The CrystalDiffract software was then used to compare the obtained intensity data with the relevant theoretical patterns from the Inorganic Crystal Structure Database (ICSD). The patterns used to index the phases were  $\beta$ -Ti (ICSD- 653278 [23]) for BCC and  $\text{Cr}_2\text{Ta}$  (ICSD-106523 [24]) for the C15 Laves phase, with minor lattice parameter alterations employed to obtain good matching.

Nanoindentation was carried out on an Agilent G200 nanoindenter with a Berkovich diamond indenter tip. Basic nanoindentation was completed to measure the hardness and modulus using the continuous stiffness measurement (CSM) method [25,26], with a depth limit of  $2\text{ }\mu\text{m}$ , an indentation strain rate at  $0.05\text{ s}^{-1}$ , a frequency of 45 Hz, a harmonic amplitude of 2 nm, and a value of 0.3 taken for Poisson's ratio. At least 9 indents were performed on each sample. Nanoindentation hardness mapping ( $\sim 3\text{ s/indent}$ ) was carried out using the Express Test function with a Berkovich tip to measure the mechanical properties of individual phases within the multi-phase alloys. at an indent spacing of 800 nm, and fixed at a target depth of 80 nm giving a maximum load of 2.25 mN. This corresponds to a depth/spacing ratio of  $\sim 1:10$ , high enough to minimise the influence of neighbouring indents as suggested by Phani and Oliver [27]. Each individual map is  $75 \times 75$  pixels or  $60 \times 60\text{ }\mu\text{m}^2$ . In the Express tests, the hardness and modulus were calculated using the Oliver and Pharr method [28] by fitting the unloading portion of the load-displacement curve. This is a different analysis method from the CSM method used for the basic nanoindentation measurements. This different analysis, plus the different strain rates, and indent sizes in the two methods may lead to systematic differences in the hardness and modulus values [29].

Scanning electron microscopy (SEM) imaging, energy dispersive X-ray spectroscopy (EDS) analysis using the Oxford Instrument XmaxN 150 EDS detector, and electron backscatter diffraction (EBSD) analysis using the Oxford Instrument Nordlys Max detector was performed on a Zeiss Crossbeam 540 dual-beam instrument. In order to reduce the overall experimental time while getting microstructural information at multiscale, we performed coarse EBSD/EDX scans (step size  $1.0\text{--}1.5\text{ }\mu\text{m}$ ) for a larger area and fine scans (step size of  $100\text{--}150\text{ nm}$ ) for a smaller area on each sample. The microstructures were also imaged using forescatter detectors (FSD) mounted below the EBSD screen.

Note that, to reveal the micro-segregation, it would be necessary to quantify the measured EDX raw intensities into elemental atomic concentrations (at%). Fig. 1 shows an example of how different conclusions on the micro-segregation behaviour in the as-cast Ti-V-Cr5-Nb-Ta alloy can be drawn using different plotting modes. From the raw intensity line scan, it can be seen the interdendritic regions (show dark contrast in the SEM image) show higher intensities of Ti, V, Cr and Nb and a misleading conclusion may be further drawn that Nb tends to be co-located with the three lighter elements Ti, V and Cr in this alloy. However, the atomic concentration profiles show that Nb is co-located with Ta and enriched in the dendritic regions. As was proposed by Castaing [30], the primary generated intensities of characteristic X-ray are roughly proportional to the respective

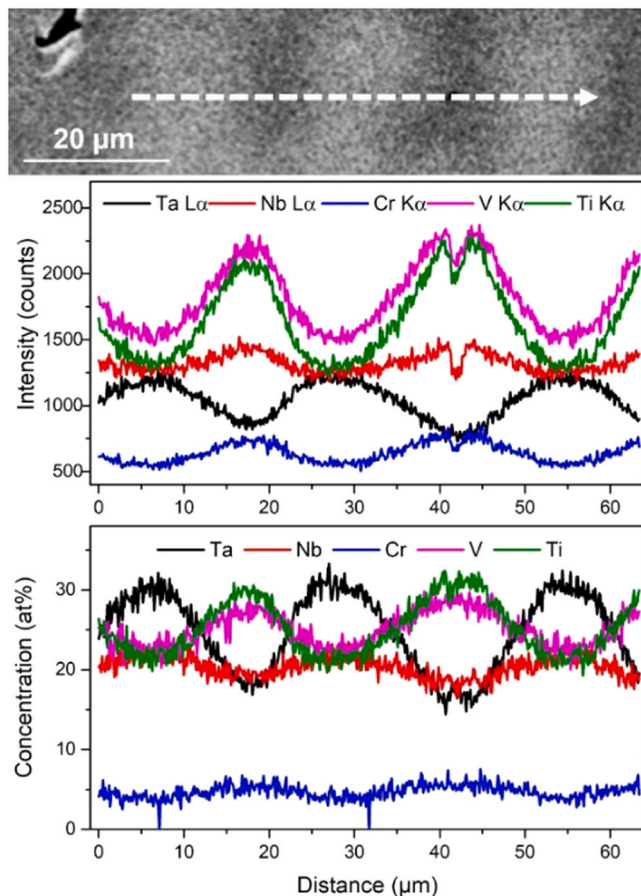


**Fig. 1.** EDX raw intensity linescan and quantline (at%) from the as-cast Ti-V-Cr5-Nb-Ta sample. Note the red lines associated with Nb show different apparent enrichment behaviour in the raw intensities and atomic concentration profiles.

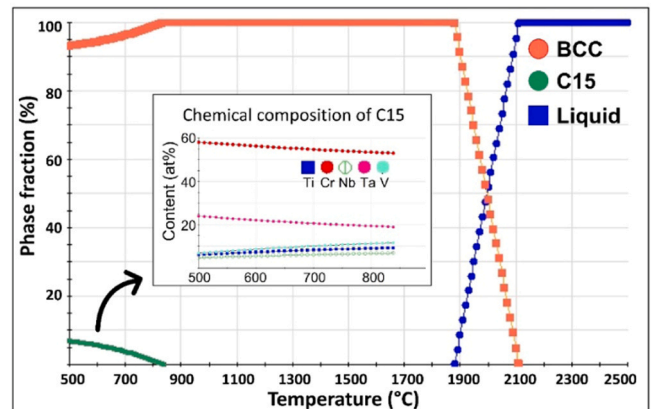
weight fractions of the emitting element. Nb has its atomic mass close to the average atomic mass of the material, leading to the possibility that a volume showing higher X-ray intensities of Nb  $L\alpha$  (or higher weight concentration of Nb) can actually possess a lower atomic concentration of Nb than its nearby regions. In the following content, all the EDX maps are shown in atomic concentration (at%) to avoid the potential misinterpretation of the Nb signal.

## 4. Results and discussion

### 4.1. Phase prediction

The calculated equilibrium phase diagrams of the Ti-V-Cr5-Nb-Ta and Ti-V-Cr-Nb-Ta RHEAs by JMatPro® are shown in Fig. 2. According to the phase diagram, Fig. 2(a), Ti-V-Cr5-Nb-Ta starts to melt at approximately 1900 °C, and exhibits a single-phase BCC structure within the temperature range from 850 °C to 1900 °C. For temperatures under approximately 850 °C, C15 Laves phase can form and its equilibrium fraction increases with further reduction in temperature. With a higher content of Cr, Ti-V-Cr-Nb-Ta possesses a lower melting point than Ti-V-Cr5-Nb-Ta, and starts to show liquid phase at around 1650 °C, Fig. 2(b). Ti-V-Cr-Nb-Ta also shows a narrower single-phase range and a wider dual-phase range compared to Ti-V-Cr5-Nb-Ta. The C15 Laves phase in Ti-V-Cr-Nb-Ta can exist at the temperatures up to 1480 °C, which possesses a higher thermal stability than that in Ti-V-Cr5-Nb-Ta. As shown in the Fig. 2(a and b inserts), the C15 Laves phase in these two alloys shows similar chemical composition as a function of temperature. The Cr content

### (a) Ti-V-Cr5-Nb-Ta



### (b) Ti-V-Cr-Nb-Ta

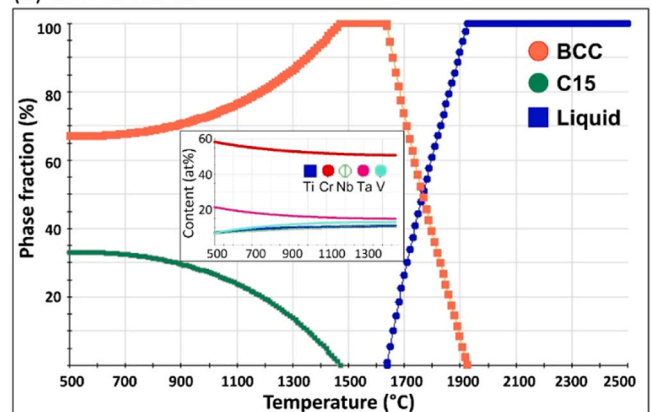


**Fig. 2.** Calculated equilibrium phase diagram for (a) Ti-V-Cr5-Nb-Ta and (b) Ti-V-Cr-Nb-Ta RHEAs by JMatPro®. The insert images show the predicted composition of the C15 Laves phase as a function of temperature.

in the C15 Laves phase at 500 °C is predicted to be ~60 at%, which decreases slightly with increasing temperatures.

In this study, the as-cast alloys were homogenised at 800 °C and 1200 °C respectively. At 800 °C, equilibrium phase diagrams indicate both alloys will exhibit a dual-phase microstructure (BCC + C15). At 1200 °C, Ti-V-Cr-Nb-Ta is expected to show dual phases while Ti-V-Cr5-Nb-Ta will exhibit a single-phase BCC microstructure.

### 4.2. Microstructural characterisation

The XRD patterns of Ti-V-Cr5-Nb-Ta and Ti-V-Cr-Nb-Ta RHEAs can be seen in Fig. 3. Bragg peaks show the presence of only a BCC phase in the as-cast Ti-V-Cr5-Nb-Ta and Ti-V-Cr-Nb-Ta. After the 800 °C heat-treatment, both alloys exhibit a dual-phase (BCC + C15) microstructure. Note that the BCC peak positions in both alloys have shifted leftwards towards smaller  $2\theta$  values after the 800 °C treatment, and it is observed Ti-V-Cr-Nb-Ta has a larger shift distance than Ti-V-Cr5-Nb-Ta, indicating Ti-V-Cr-Nb-Ta has a larger change in BCC lattice parameter. After the 1200 °C treatment, Ti-V-Cr5-Nb-Ta shows a single-phase BCC structure with the lattice parameters close to the as-cast. A few peaks are labelled in the XRD pattern of the 1200 °C homogenised Ti-V-Cr5-Nb-Ta sample, from the medium used to hold the samples securely in place [5]. The grain size is ~hundreds of  $\mu\text{m}$ , which leads to difference in relative peak intensities, e.g. (011) and (002) vary from sample to sample. Ti-V-Cr-Nb-Ta after ageing at 800 °C and 1200 °C shows dual-phase patterns (BCC + C15) similar to the 800 °C homogenised Ti-V-Cr5-Nb-Ta sample. For both alloys, the width of the BCC phase peaks tends to be

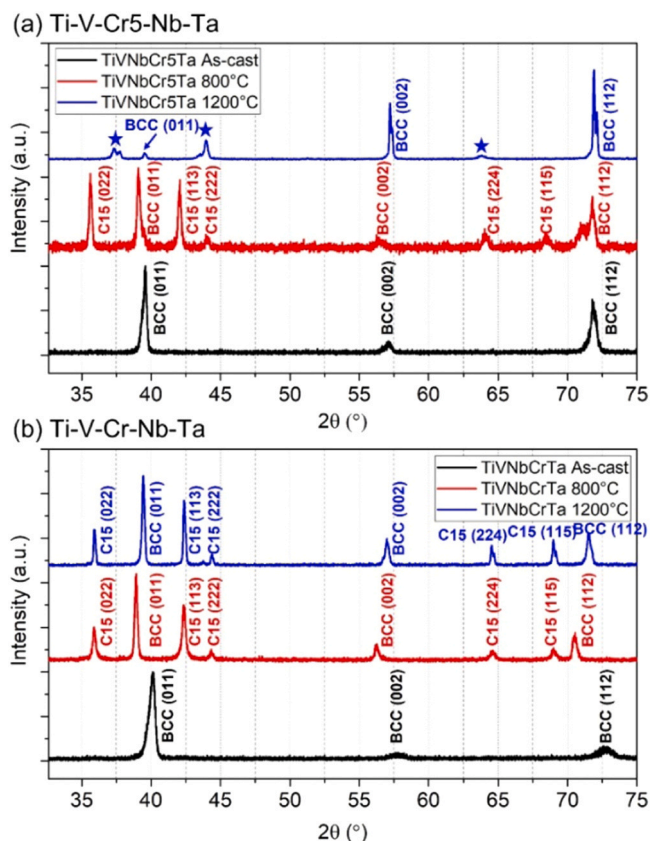


**Fig. 3.** XRD patterns of the (a) Ti-V-Cr5-Nb-Ta and (b) Ti-V-Cr-Nb-Ta RHEAs. The peaks from the medium used to hold the samples are labelled with stars.

broader for the as-cast condition than for the two heat-treated conditions.

Figs. 4 and 5 show the co-located FSD images, EDX elemental maps, EBSD band contrast, and EBSD phase maps for the Ti-V-Cr5-Nb-Ta alloy. In FSD images, the region with an enrichment of heavier elements or with a higher average atomic mass will present a brighter contrast. The dendritic regions in the as-cast sample show bright contrast while the interdendritic regions are darker, indicating that elemental segregation occurs during the solidification process, Fig. 4(a-1). The elemental distributions of dendritic and interdendritic regions were further examined by the EDX elemental mapping. This indicates that Ta and Nb segregate preferentially to the dendritic regions, and the interdendritic regions are enriched in the lower melting point and lighter elements, Ti, V and Cr. The micro-segregation of Cr and Nb can be seen more obviously from the quantline in Fig. 1. In Fig. 4(a-8) and 5 (a-8), EBSD phase maps indicate the as-cast Ti-V-Cr5-Nb-Ta alloy forms a single-phase BCC structure which agrees with the XRD result. The black dots in the EBSD maps reflect the presence of porosity in the as-cast alloy.

There appears to be coring of the dendrites, with an enrichment of lighter elements away from the centre of the dendrite after the 800 °C homogenisation treatment. This can be seen from the FSD image in Fig. 4(b). EDX analysis shows that the interdendritic regions still possess an enrichment of light elements Ti, V and Cr. After homogenisation, the dendritic regions are indexed as a single-phase BCC structure, but the interdendritic regions show poor band qualities, which are shown as dark contrast in the band contrast maps, Fig. 4(b-7). Finer-scale EDX/EBSD scans were performed at the dendrite boundaries to further check the elemental and phase distribution, as highlighted in Fig. 5(b). The results indicate there are nano-scale V- and Cr-enriched precipitates formed in the interdendritic regions and some of these precipitates are indexed as C15

Laves phase, Fig. 5(b). As shown in some higher-magnification SEM images in next section, Fig. 9(a), there are at least two types of nano-precipitates formed in the interdendritic region in the 800 °C homogenised Ti-V-Cr5-Nb-Ta sample. Some of these nano-precipitates are below the resolution of SEM-based techniques (e.g. EDX and EBSD) and will need future Transmission Electron Microscopy (TEM) or Atom Probe Tomography (APT) to provide structural and chemical information.

To obtain a fully-homogeneous elemental distribution, the Ti-V-Cr5-Nb-Ta sample was subject to a high temperature heat treatment at 1200 °C. This thermal treatment results in the complete elimination of the dendritic structure as observed in Fig. 4(c). The EDX measurements at both coarse and finer scales further confirm the homogeneous chemical distribution in the sample heat-treated at 1200 °C for 48 hrs. The black dots in the EBSD maps, Fig. 4(c-7) and (c-8), again originate from the pores in the alloy, which can also be seen in the FSD image Fig. 4(c-1). The 1200 °C homogenised Ti-V-Cr5-Nb-Ta exhibits a single-phase BCC structure, and EBSD maps show that there is no formation of other detectable phases along the grain boundary nor inside the grain, as indicated in Fig. 4(c-8) and 5 (c-8).

Figs. 6 and 7 show the co-located FSD images, EDX elemental maps, EBSD band contrast, and EBSD phase maps for the Ti-V-Cr-Nb-Ta alloy. The as-cast alloy shows similar microstructure to as-cast Ti-V-Cr5-Nb-Ta in Fig. 4(a), with Ta and Nb enriched dendritic regions and Ti, V and Cr in the interdendritic regions. Some casting porosity with dark contrast can be seen from the EBSD maps. The as-cast alloy exhibits a major BCC phase structure with a small fraction of nano-scale precipitates along the grain boundary, Fig. 6(a-8) and 7 (a-8). EBSD and EDX results indicate that these precipitates are Cr-enriched C15 Laves phase. The chemical composition of C15 Laves phase in different samples is summarised in Table 5 and will be discussed in the Discussion Section. The Ti-V-Cr-Nb-Ta alloy probably formed a single-phase BCC microstructure immediately after solidification, and decomposed into BCC + C15 at grain boundaries in the solid-state during cooling, with the boundaries acting as the low energy heterogeneous nucleation sites.

Heat treatment at 800 °C for 48 hrs of Ti-V-Cr-Nb-Ta led to an improved degree of chemical homogeneity compared to the as-cast state but not fully homogenous, as shown in the FSD images in Fig. 6(a-1) and (b-1). Similar to the Ti-V-Cr5-Nb-Ta alloy, the interdendritic regions in 800 °C homogenised Ti-V-Cr-Ta-Nb also exhibit poor band qualities as shown in the coarse-scan EBSD band contrast map in Fig. 6(b-7). The finer-scan EDX and EBSD maps in Fig. 7(b) have covered both the interdendritic and dendritic regions, and it is revealed that the interdendritic regions underwent phase segregation resulting in a high density of C15-Laves precipitates. These precipitates have a relatively high concentration of V, Cr and Ta and are depleted of Ti and Nb. The interdendritic region was single-phase after solidification, and decomposed into the BCC and C15 Laves phases in the solid-state during homogenisation treatment, Fig. 7(a-8) and (b-8).

Annealing at 1200 °C resulted in the complete elimination of the dendritic features in Ti-V-Cr-Nb-Ta, Fig. 6(c). A large volume fraction (~34%) of C15 Laves phase are seen uniformly distributed in the BCC matrix, Fig. 6(c), in agreement with the XRD result in Fig. 3. The finer-scan EDX/EBSD maps show these C15-Laves precipitates are V-, Cr- and Ta- enriched, and Ti- and Nb- depleted and the average grain size of C15-Laves precipitates size is 1 μm with a standard deviation of 0.55 μm, Fig. 7(c).

The characterisation of elemental and phase segregations in the two alloys with different heat-treatment conditions is summarised in Table 3. The only sample which was successfully homogenised and exhibited a single-phase structure is the Ti-V-Cr5-Nb-Ta after it underwent the 1200 °C treatment, as for the other samples, residual dendrites or formation of C15 Laves phase was observed. The phase

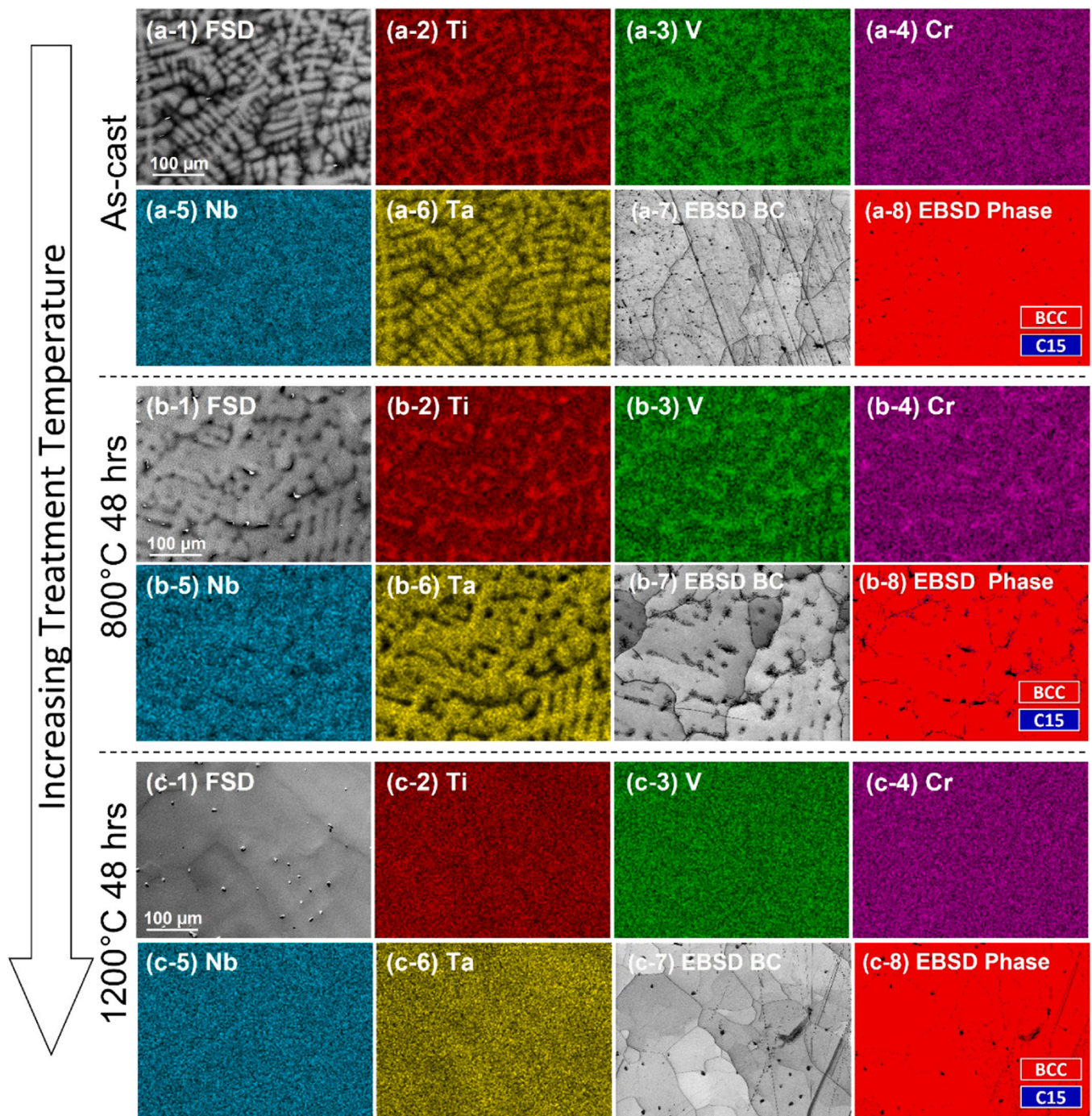


**Fig. 4.** Co-located coarse FSD, EDX and EBSD scans showing microstructural evolutions of Ti-V-Cr5-Nb-Ta in (a) as-cast, (b) 800 °C homogenised and (c) 1200 °C homogenised conditions. Elemental concentration is directly reflected by the colour intensity in the EDX maps.

fractions of C15 Laves phase in Table 3 were calculated from the finer EBSD scans in Figs. 5 and 7. It is possible that the C15 Laves phase fraction in the bulk material is lower than the values here due to the small EBSD sampling area, but it is also possible that C15 Laves phase of smaller size may be present but not detected.

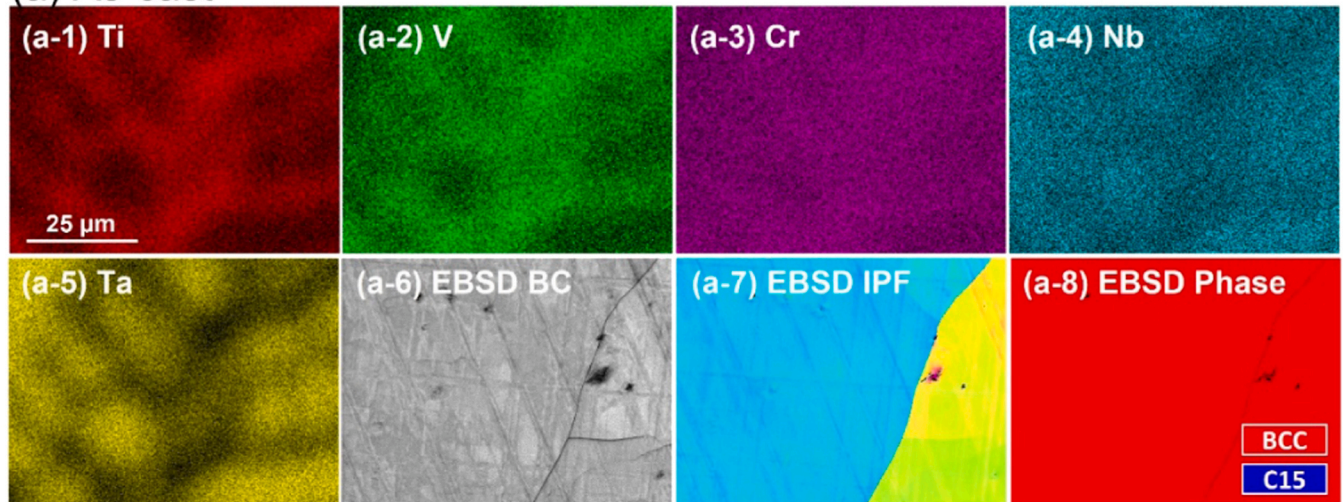
#### 4.3. Nanoindentation hardness and modulus

Hardness and modulus were calculated from the nanoindentation CSM data. The hardness-modulus plot (H-E plot) for the two alloys investigated in this study, Ti-V-Cr5-Nb-Ta and Ti-V-Cr-Nb-Ta is shown in Fig. 8, which shows each measurement with markers, and

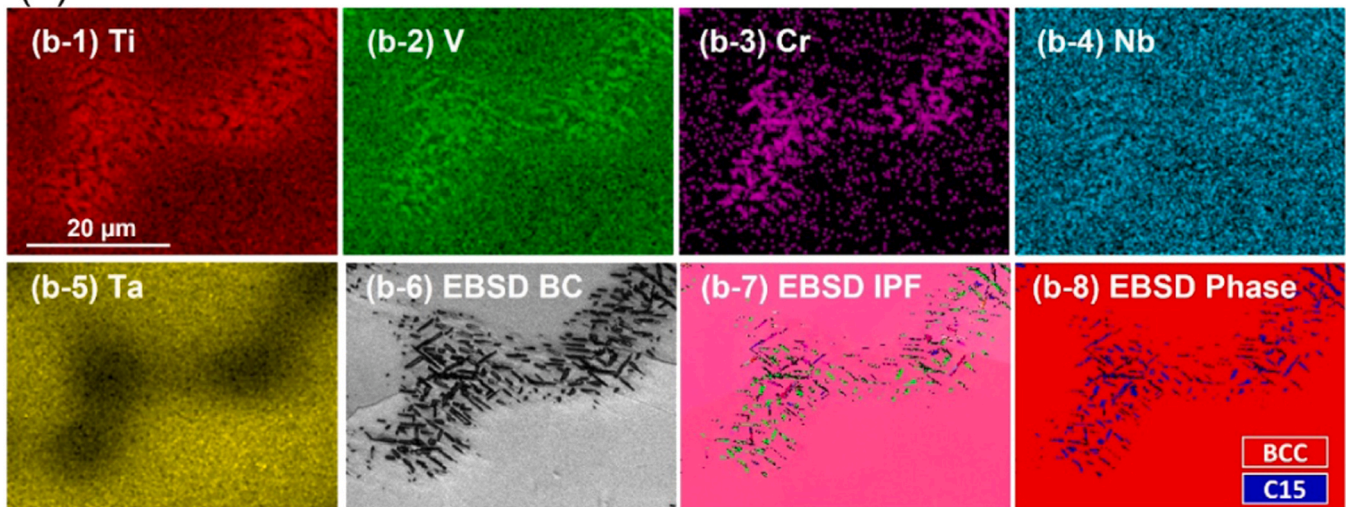
envelopes the markers of each sample in a 95% confidence bound ellipse. Lee et al. [2] and Scales [31] have investigated the mechanical properties and microstructure of equiatomic Ti-V-Nb-Ta alloys. As a comparison, hardness and modulus values for the Ti-V-Nb-Ta alloy from a previous study [31] are also included in Fig. 8.

The size and location of the ellipses demarking 95% confidence regions vary from the bottom left-hand corner of the plot when the microstructure is primarily single-phase BCC and goes towards the top right-hand corner where a higher fraction of C15 Laves phase is formed. Ti-V-Nb-Ta exhibits similar microstructure in the as-cast and the 800 °C homogenised conditions with a single-phase BCC microstructure and inhomogeneous elemental distribution [2,31],

## (a) As-cast



## (b) 800°C 48 hrs



## (c) 1200°C 48 hrs

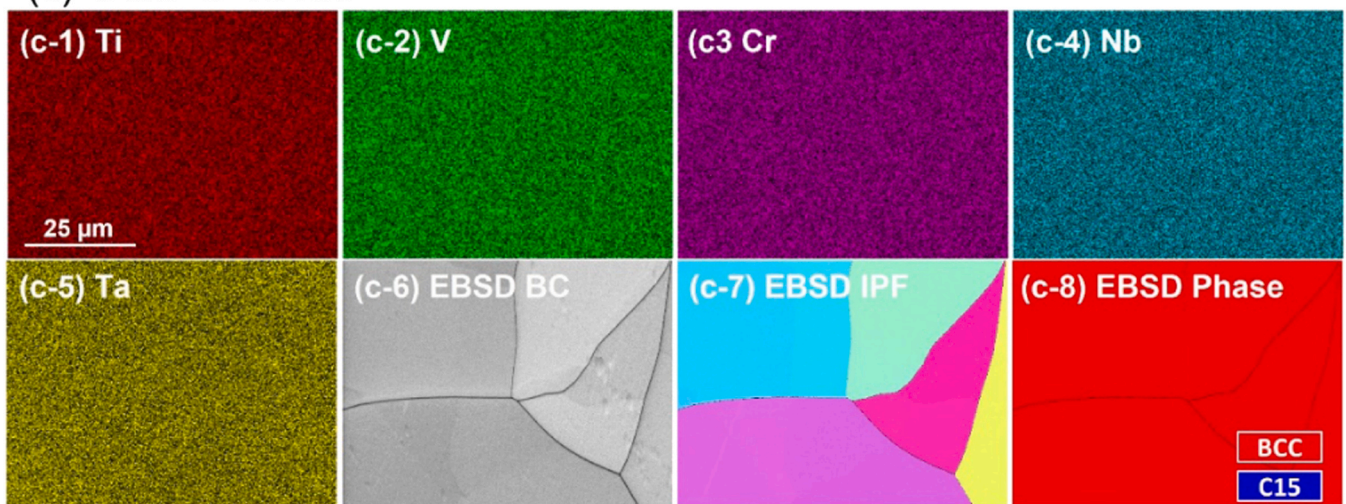


**Fig. 5.** Co-located finer EDX and EBSD scans showing microstructural evolutions of Ti-V-Cr5-Nb-Ta in (a) as-cast, (b) 800 °C homogenised and (c) 1200 °C homogenised conditions.

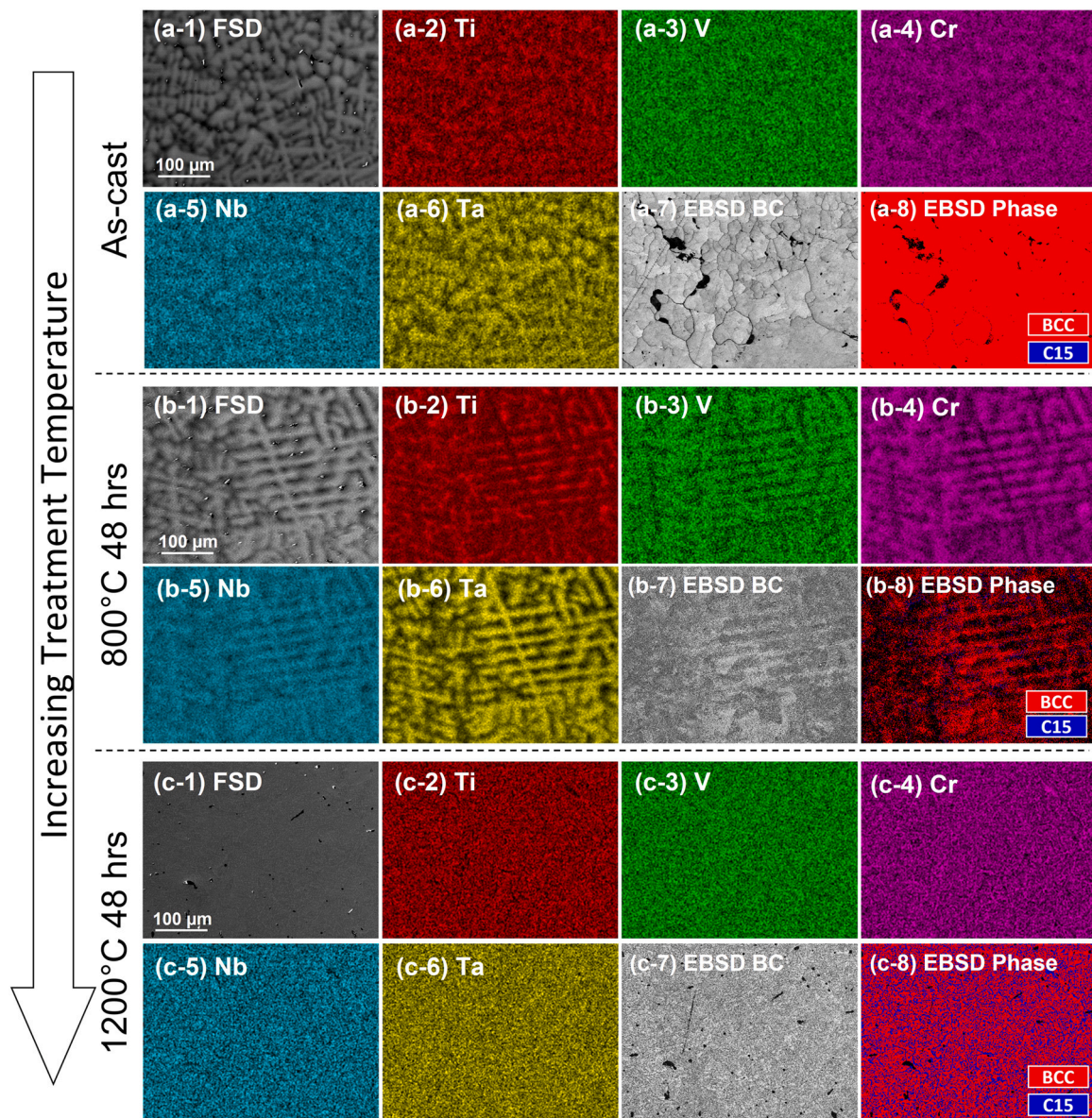


**Fig. 6.** Co-located coarse FSD, EDX and EBSD scans showing microstructural evolutions of Ti-V-Cr-Nb-Ta in (a) as-cast, (b) 800 °C homogenised and (c) 1200 °C homogenised conditions.

which concurs with the similar statistics of hardness and modulus observed in these two samples. However, the 1200 °C heat treatment developed a fully-homogeneous single phase solid-solution microstructure in Ti-V-Nb-Ta, which led to smaller scatter in the indentation data and an increased hardness by ~17% relative to the as-cast and 800 °C homogenised Ti-V-Nb-Ta.

The hardness of Ti-V-Cr5-Nb-Ta in as-cast, 800 °C homogenised and 1200 °C homogenised conditions increases by 11.9%, 20.2% and 15.7% relative to the Cr-free Ti-V-Nb-Ta alloy, while the modulus also increases by 1.4%, 1.7% and 9.8% respectively. Ti-V-Cr5-Nb-Ta alloy exhibits larger variations in the indentation data for the as-cast and 800 °C homogenised conditions compared to the Ti-V-Nb-Ta alloy, which can be attributed to the higher degree of chemical inhomogeneity by adding Cr and the formation of C15-Laves precipitates observed in the 800 °C homogenised sample. Of the two Cr-containing alloys investigated in this paper, the 1200 °C homogenised Ti-V-Cr5-Nb-Ta is the only sample that achieves a fully homogeneous single-phase solid-solution microstructure, and shows the smallest variations in hardness and modulus.

Ti-V-Cr-Nb-Ta exhibits the highest hardness and modulus among the three alloys. The hardness of Ti-V-Cr-Nb-Ta is increased by 45.2%, 93.8% and 89.3% in the as-cast, the 800 °C homogenised and the 1200 °C homogenised state respectively, relative to the Ti-V-Nb-Ta alloy. This is consistent with the microstructural characterisation in Section 4.2 showing a high fraction of C15 Laves phase in the homogenised Ti-V-Cr-Nb-Ta alloys.

To further explore the interrelationship between local microstructure and hardness and understand the hardening mechanisms in the RHEAs, correlative nanoindentation mapping and back-scattered electron (BSE) imaging were performed on selected samples. The correlative BSE images, hardness and modulus maps from the 800 °C homogenised Ti-V-Cr5-Nb-Ta and the 1200 °C homogenised Ti-V-Cr-Nb-Ta are shown in Fig. 9. Each hardness/modulus map in Fig. 9 covers  $60 \times 60 \mu\text{m}^2$  area and consists of 5625 indents. The hardness variation across different regions in the two samples is clearly captured by the maps, indicating that the indent spacing is sufficient to capture the key microstructural features. In order to determine the mechanical properties of specific regions/phases, the

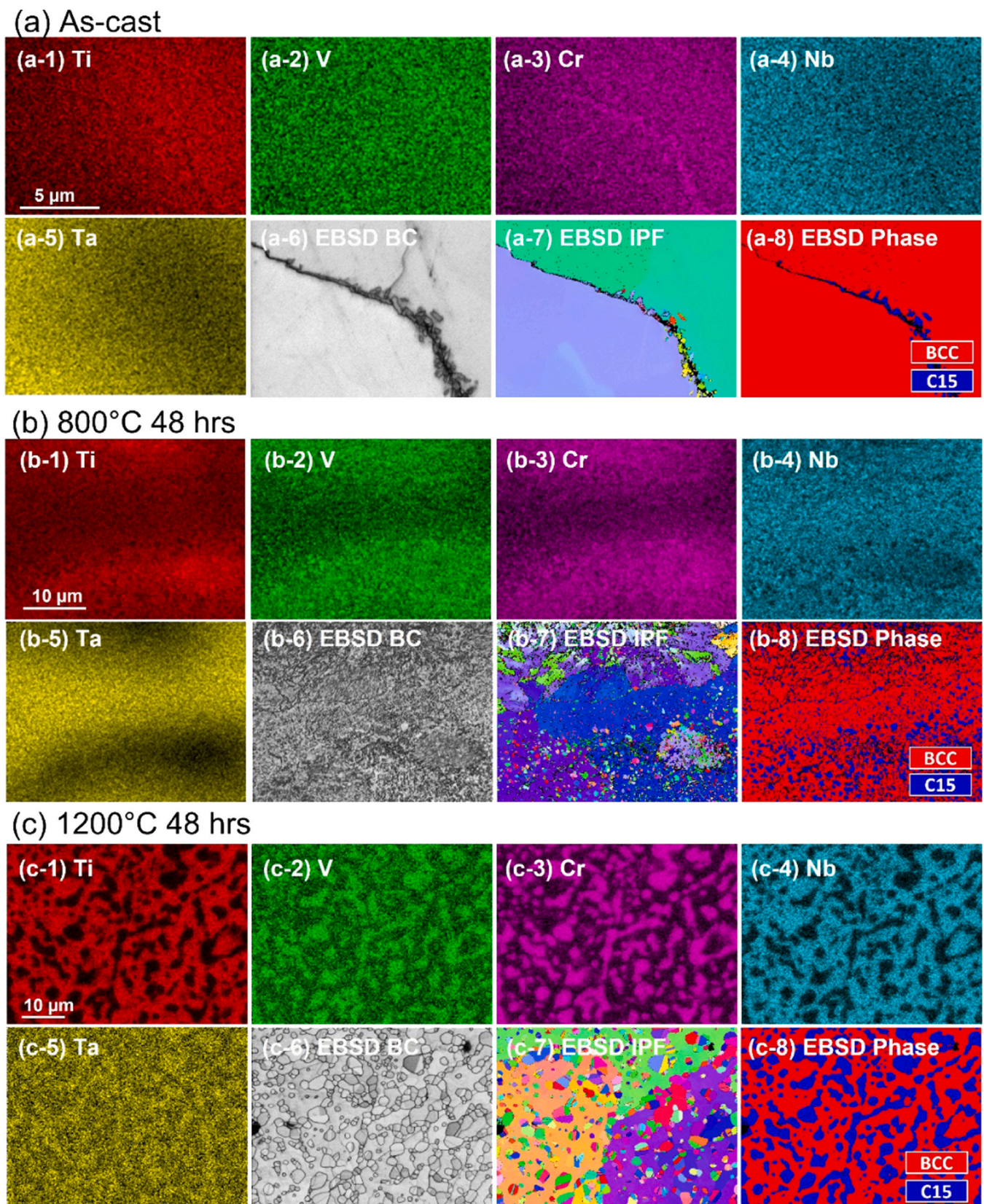


**Fig. 7.** Co-located finer EDX and EBSD scans showing microstructural evolutions of Ti-V-Cr-Nb-Ta in (a) as-cast, (b) 800 °C homogenised and (c) 1200 °C homogenised conditions.

**Table 3**

A summary of micro-segregation and phase distributions in the two alloys.

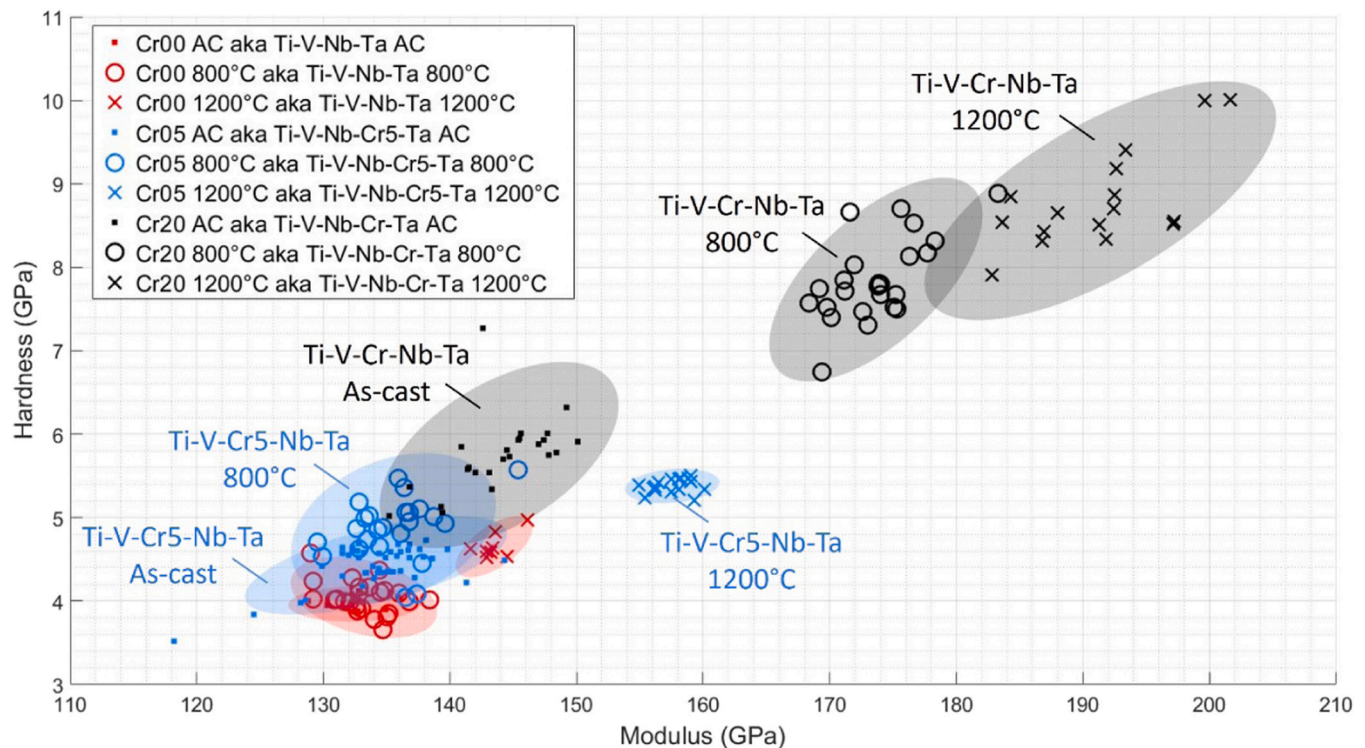
Alloy		Micro-segregation	Phase segregation	C15 phase fraction
Ti-V-Cr5-Nb-Ta	As-cast	Dendrites	BCC	–
	800 °C	Dendrites	BCC + C15 (within interdendrites)+ undefined precipitates	2.65%
	1200 °C	No dendrites	BCC	–
Ti-V-Cr-Nb-Ta	As-cast	Dendrites	BCC + C15 (at some GBs)	1.93%
	800 °C	Dendrites	BCC + C15 (most in interdendrites) + undefined precipitates	16.93%
	1200 °C	No dendrites	BCC + uniformly distributed C15	34.27%

indentation mapping data has to be deconvoluted based on micro-structural features. Histograms and statistics of the hardness and modulus deconvoluted for specific regions/phases are shown in Fig. 10.

Fig. 9(a) shows a typical region before the indentation test in the 800 °C homogenised Ti-V-Cr5-Nb-Ta. Comparison of Fig. 9(a) and (c) shows that the interdendritic region with a high density of C15-Laves nano-precipitates exhibits a higher level of hardness relative to the surrounding dendritic region. The interdendritic regions have an average hardness of 7.6 GPa, which is 15% higher than the average value of the surrounding dendrite. The nanoindentation mapping shows little difference in modulus between the dendrite and interdendritic regions, Fig. 9(c), which is further confirmed by the overlapping peaks in the histogram in Fig. 10 (and b). Fig. 9(b) shows the microstructure in the 1200 °C homogenised Ti-V-Cr-Nb-Ta alloy, and a high fraction of C15 Laves phase can be seen. The C15 Laves phase

shows significantly higher hardness and modulus compared to the surrounding BCC matrix, Fig. 9(d and f). When the indentation hardness and modulus are plotted as histogram, Fig. 10 (c and d), two distinct peaks are visible. The mean value of each peak represents the mean hardness of the respective phase. The matrix has a mean hardness of 7.4 GPa and modulus of 172.3 GPa. The C15 Laves phase is hard and elastically stiffer, having a mean hardness of 14 GPa and modulus of 223.5 GPa.

The average hardness and modulus of the 800 °C homogenised Ti-V-Cr5-Nb-Ta and 1200 °C homogenised Ti-V-Cr-Nb-Ta measured by the nanoindentation mapping in Fig. 10 are observed to be higher than that from the basic indentation measurements (or CSM measurements) in Fig. 8. This discrepancy may be related to the rate at which the indents were performed, the indent size effect, or due to the difference in the way these values are calculated in the two indentation methods [29]. In that case, the hardness and modulus



	Ti-V-Nb-Ta		Ti-V-Cr5-Nb-Ta		Ti-V-Cr-Nb-Ta	
	Hardness (GPa)	Modulus (GPa)	Hardness (GPa)	Modulus (GPa)	Hardness (GPa)	Modulus (GPa)
As-cast	3.96 ± 0.09	132.4 ± 2.1	4.43 ± 0.24	134.2 ± 4.2	5.75 ± 0.46	143.9 ± 3.9
800 °C	4.05 ± 0.2	133.2 ± 2.4	4.87 ± 0.37	135.5 ± 3.3	7.85 ± 0.5	173.6 ± 3.4
1200 °C	4.65 ± 0.15	143.5 ± 1.3	5.38 ± 0.08	157.6 ± 1.5	8.8 ± 0.58	191.4 ± 5.7

**Fig. 8.** Nanoindentation hardness and modulus of as-cast and homogenised samples. The ellipses contain 95% of the measurements. The average hardness and modulus with standard deviation are derived from the CSM data.

Cr05 and Cr20 represent Ti-V-Cr5-Nb-Ta and Ti-V-Cr-Nb-Ta alloys investigated in this paper and the datasets for Ti-V-Nb-Ta are adapted from [31].

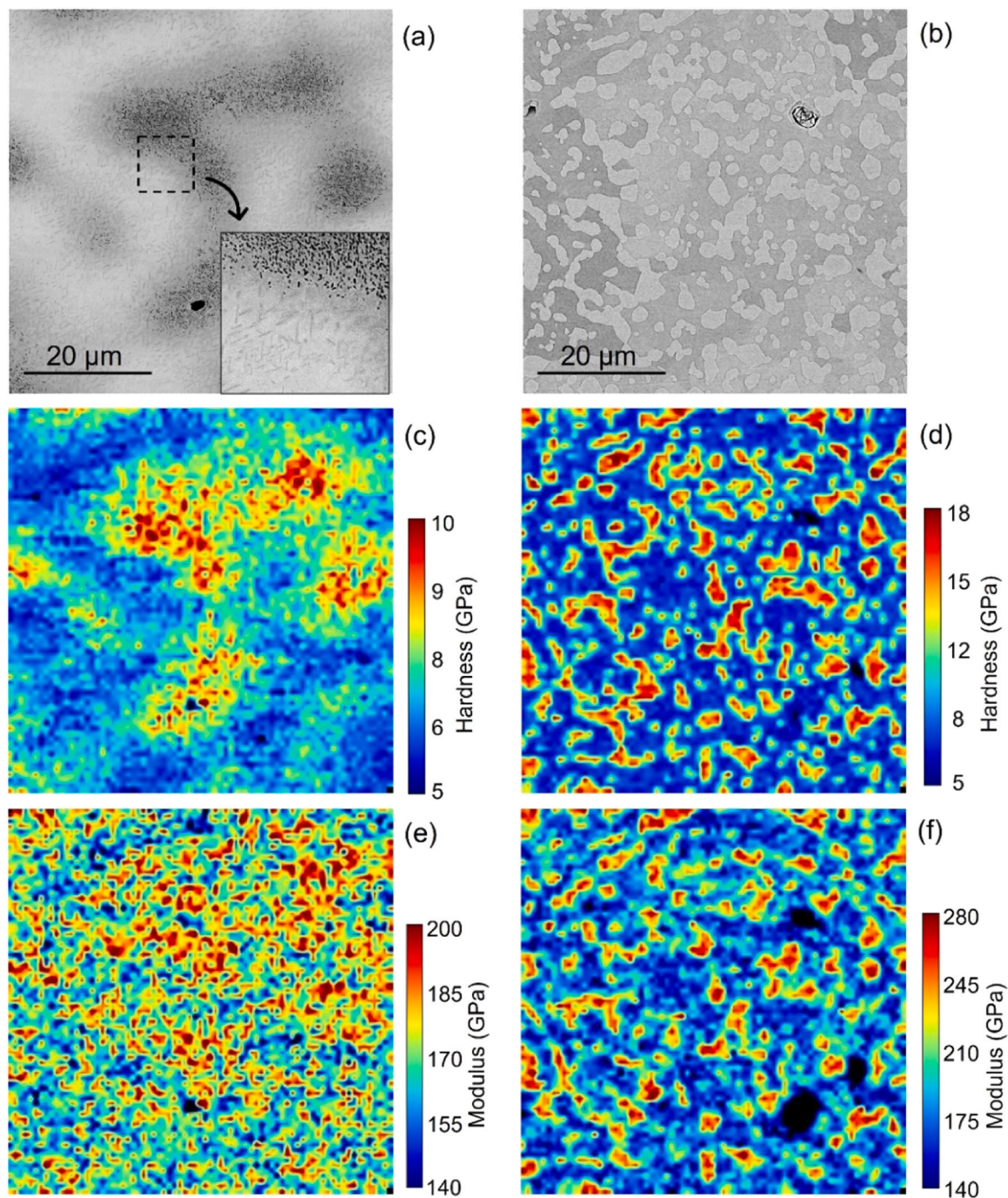


**Fig. 9.** Correlative BSE, nanoindentation hardness and modulus maps for (a, c and e) 800 °C homogenised Ti-V-Cr5-Nb-Ta and (b, d and f) 1200 °C homogenised Ti-V-Cr-Nb-Ta alloys. The insert image in (a) shows a high density of nano-precipitates in the interdendritic region.

measured from the two different methods cannot be compared directly, but comparisons of hardness changes measured using the same method remain valid.

## 5. Discussions

### 5.1. Micro-segregation

The partition coefficient,  $K = C_{dr}/C_{idr}$  [32], has been widely used to quantitatively evaluate the micro-segregation behaviours of the alloying elements in as-cast RHEAs [33–35], where  $C_{dr}$  and  $C_{idr}$  are the average concentrations (at%) of the centres of dendrite arms and

interdendritic regions respectively. The  $K$  value of an alloying element, which reflects the correlation of the excess/deficiency of the concentration in the dendrite arms, is often associated with its melting temperature [34,35]. Elements with melting points higher than the average melting temperature of the materials  $T_m^{mix} = \sum c_i(T_m)_i$ , where  $c_i$  is the atomic concentration of an alloying element  $i$  and  $T_m$  is its corresponding melting temperature), or  $K > 1$ , tend to solidify first and segregate to the centre of the dendrites. Low melting point elements, or  $K < 1$ , will be then rejected into the melt and solidify at the interdendritic regions [36,37]. The average melting temperature together with the partition coefficients for the two alloys in as-cast conditions are summarised in Table 4. In both

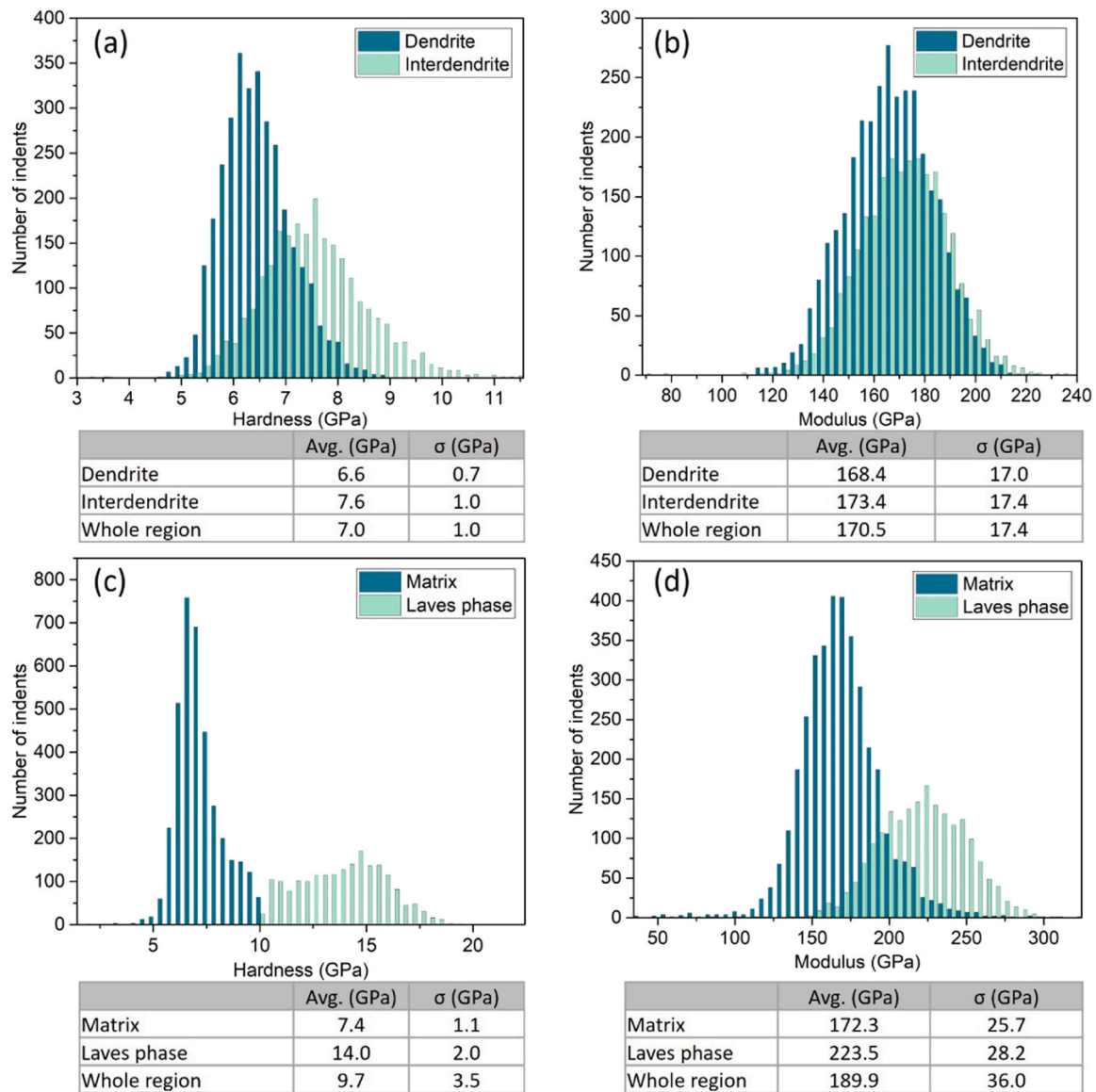


**Fig. 10.** Histograms and statistics of hardness and modulus obtained in Fig. 9, (a, b) the 800 °C homogenised Ti-V-Cr5-Nb-Ta and (c, d) the 1200 °C homogenised Ti-V-Cr-Nb-Ta.

alloys investigated, Ta and Nb have  $K$  values higher than 1 and are observed to be enriched in the dendritic regions. The lower melting temperature elements Ti, V and Cr are preferentially co-located and enriched in the interdendritic regions. The co-located behaviour of Nb and Ta in as-cast RHEAs observed here is in agreement with the observations reported by Couzinié et al. [37] and Yao et al. [34] in as-cast Ti-Zr-Hf-Nb-Ta and Ti-V-Nb-Ta-W alloys respectively. In Cr ( $x = 0.5, 1.0$  and  $2.0$ )-Mo-Nb-Ta-V-W alloys, Zhang et al. [33] reported

the co-locations of Nb with Cr and V rather than Ta and W. That is because the RHEAs investigated by Zhang et al. [33] all possess higher average melting temperatures than Nb.

## 5.2. Strengthening effect

With the increase of Cr content, the nano-hardness for as-cast Ti-V-Cr<sub>x</sub>-Nb-Ta ( $x = 0, 5$  or  $20$  at%) increases from 3.96 GPa to 5.75 GPa.

**Table 4**

The average concentrations (at%) at the centres of dendrite arms,  $C_{dr}$ , and interdendritic regions,  $C_{idr}$ , and the partition coefficient  $K$  in the as-cast alloys.

Alloy	$T_m^{mix}$ (°C)		Ti	V	Cr	Nb	Ta
Ti-V-Cr5-Nb-Ta	2239.5	$C_{dr}$	$20.65 \pm 0.49$	$21.18 \pm 0.71$	$3.57 \pm 0.27$	$22.56 \pm 0.41$	$32.04 \pm 1.01$
		$C_{idr}$	$31.98 \pm 0.8$	$28.9 \pm 0.4$	$6.11 \pm 0.23$	$17.91 \pm 0.44$	$15.11 \pm 0.96$
		$K$	0.65	0.73	0.58	1.26	2.12
Ti-V-Cr-Nb-Ta	2195.8	$C_{dr}$	$18.16 \pm 0.48$	$17.82 \pm 0.18$	$17.15 \pm 0.62$	$22.32 \pm 0.34$	$24.55 \pm 0.78$
		$C_{idr}$	$24.88 \pm 0.84$	$19.85 \pm 0.17$	$22.63 \pm 0.56$	$18.18 \pm 0.47$	$14.46 \pm 0.98$
		$K$	0.73	0.90	0.76	1.23	1.70

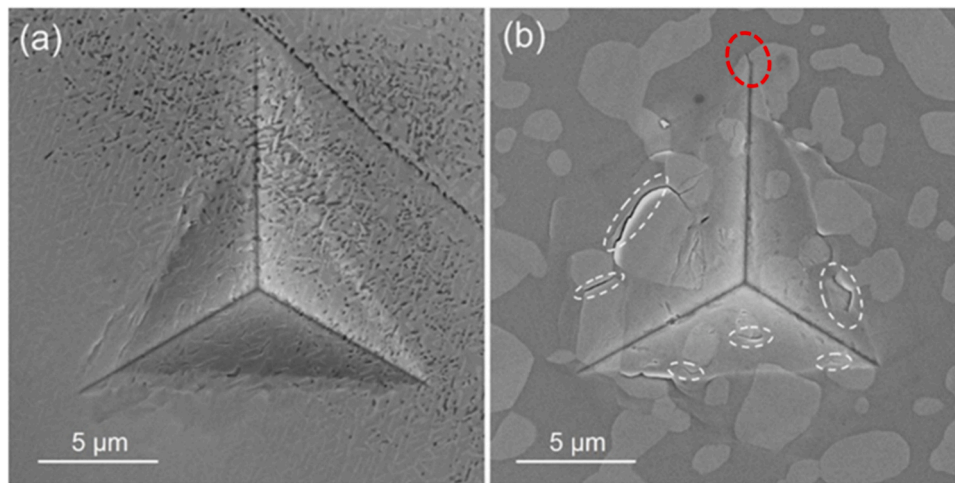


**Fig. 11.** The SEM images of nanoindentation taken from (a) the 800 °C homogenised Ti-V-Cr5-Nb-Ta and (b) 1200 °C homogenised Ti-V-Cr-Nb-Ta. The cracks are labelled by the dashed ellipses: white for interfacial cracks, and red for transverse cracks.

All three RHEAs offer a comparable or higher hardness relative to conventional structural materials, such as 301SS [38] and Fe-Cu alloys [39]. As-cast Ti-V-Nb-Ta and Ti-V-Cr5-Nb-Ta exhibit a single-phase BCC structure, while Ti-V-Cr-Nb-Ta has less than 2% volume fraction of C15-Laves precipitates mainly formed at grain boundaries. Considering the grain sizes of the materials studied are more than 200 µm, grain-boundary strengthening and precipitates strengthening in the as-cast materials can be neglected [40]. Local lattice distortions, causing solid-solution like strengthening [2,41–43], is likely to be the dominant strengthening mechanism in the as-cast Ti-V-Nb-Cr<sub>x</sub>-Ta (x = 0, 5 or 20, at%) alloys.

Lattice distortion, originating from the mixing of different sized elements in a concentrated solid solution, can result in an intrinsic residual stress field which fluctuates from one lattice site to another [41,44]. These lattice distortions or the local compositional fluctuations introduce energy barriers against dislocation motions and serve as a solid-solution like strengthening mechanism [45]. To evaluate the lattice distortions in HEAs, Zhang et al. [46] proposed to use the atomic size difference parameter ( $\delta$ ):

$$\delta = 100\% \sqrt{\sum_{i=1}^n c_i \left( 1 - \frac{r_i}{\sum_{j=1}^n c_j r_j} \right)^2}$$

in which  $c_i$  is the atomic fraction of element  $i$ ,  $r_i$  the atomic radius of element  $i$  and  $n$  the total number of constituent elements. The atomic radii used in this work were cited from [47]. Here, a larger  $\delta$  parameter indicates a higher level of atomic size mismatch or lattice distortion. The  $\delta$  parameter has been widely accepted as one of the empirical parameters to guide the design of HEAs [41,44]. Chen et al. [42] reported a linear correlation between the value of the  $\delta$  parameter and the microhardness for a series of single-phase Nb-Mo-Cr-Ti-Al alloys.

The  $\delta$  parameter values calculated for Ti-V-Nb-Ta, Ti-V-Cr5-Nb-Ta and Ti-V-Cr-Nb-Ta are 3.93%, 4.66% and 5.88% respectively. Cr has a smaller atomic radius relative to Ti, V, Nb and Ta. Increasing the content of Cr into these RHEAs can thus lead to a higher level of lattice distortion or solid strengthening, which concurs with the hardness changes. The homogenised samples without the second-phase formation possess an improved degree of chemical homogeneity compared to the as-cast state, which leads to a smaller deviation of  $\delta$  values and thus smaller variations in hardness.

At the nanometric scale, nanosized precipitates can act as direct pinning agents or cause back stresses on dislocation motion during deformation due to comprising different atomic sequence and/or

different crystal structure. As shown in Figs. 6 and 7, fine precipitates are formed in the 800 °C homogenised Ti-V-Cr5-Nb-Ta and Ti-V-Cr-Nb-Ta alloys, and these precipitates are observed to produce local hardening. However, these nano-precipitates tend to form within the interdendritic regions. Therefore, applying a suitable modification of the chemical composition of the alloy, combined with appropriate thermomechanical treatment, is required to distribute precipitates uniformly. Considering the calculated phase diagrams, Fig. 2, and the microstructural analysis above, a two-step heat treatment process is thus proposed to introduce a fine second-phase dispersion in Ti-V-Cr5-Nb-Ta. First, a high temperature annealing to achieve a fully-homogeneous single-phase microstructure for which we have demonstrated a temperature of 1200 °C for 48 h to work, but this could be optimised to other times and temperatures guided by the phase diagram, Fig. 2(a). A second heat treatment at a temperature below 850 °C can then be used to control the size and density of nano-precipitates. We have shown that precipitation occurs at 800 °C, though without the initial homogenisation step to give a uniform distribution. Optimisation of ageing time and temperature would require further study of the precipitation kinetics.

### 5.3. C15 Laves phase

The formation of C15 Laves phase particle increases the hardness and modulus for the 1200 °C homogenised Ti-V-Cr-Nb-Ta alloy by 53% and 33% respectively compared to its as-cast state. The effect of Laves phase on the mechanical properties, beneficial or detrimental, mainly depends on the volume fraction and mean size of Laves phase in the RHEAs. With increasing mean size and volume fraction of Laves phase, crack initiation and crack growth would rapidly increase [48]. In this study, small cracks can be observed around the indentations employed for the 1200 °C homogenised Ti-V-Cr-Nb-Ta sample, but not for the 800 °C homogenised Ti-V-Cr5-Nb-Ta sample, Fig. 11.

Due to the complex crystal structure, dislocations are difficult to be generated and glide within the C15 Laves phase relative to the BCC matrix, which agrees with the nanoindentation mapping results. The nanoindentation mapping indicates the C15 Laves phase is very hard and brittle. The hardness of the C15 Laves phase was measured to be  $\approx 14$  GPa, nearly 2 times that of the BCC matrix phase. The two different phases will affect the nucleation and propagation of cracks. The majority of indentation induced cracks observed in the 1200 °C homogenised Ti-V-Cr-Nb-Ta sample, Fig. 11 (b), are either at C15/BCC interfaces or C15/C15 interfaces. Occasionally, transverse cracking in the C15 phase was seen, for example at the

**Table 5**

Chemical compositions (at%) of C15 Laves phase identified in different samples.

Alloy	Conditions	Ti	V	Cr	Nb	Ta	Ti + Ta	V + Cr + Nb
Ti-V-Cr5-Nb-Ta	800 °C 48hrs	25.3	31.6	9.6	14.6	18.9	44.2	55.8
Ti-V-Cr-Nb-Ta	As-cast	15.6	19.2	32.3	16.0	16.9	32.5	67.5
	800 °C 48hrs	16.9	23.7	25.2	13.7	20.5	37.5	62.6
	1200 °C 48 hrs	12.8	23.2	31.6	11.7	20.8	33.6	66.4

\*Chemical compositions of C15 in the three samples are calculated from fine-scan EDX maps using the Analyze Phases function in Aztec with a boundary Tolerance of 5 and grouping level 1.

\*\*Chemical compositions of C15 in as cast Ti-V-Cr-Nb-Ta are calculated from EDX linescans using the QuantLine function in Aztec.

top corner of the indent in Fig. 11 (b), which then arrests at the interface with BCC matrix. The combined effect of the significant increase in hardness and formation of weak interfaces between BCC and Laves phase is likely to reduce the ductility of this alloy significantly.

The chemical composition of the C15 Laves phase in different samples is summarised in Table 5. However, due to the small size of the Laves precipitates in the samples, especially for the 800 °C homogenised Ti-V-Cr5-Nb-Ta and as-cast Ti-V-Cr-Nb-Ta sample, the EDX scans likely include some BCC matrix within their sampling volume; causing the obtained results to vary from the true composition for the C15-Laves phase.

C15 Laves phase has a stoichiometry of AB<sub>2</sub>, while all the five component elements were observed in the C15 Laves phase in Ti-V-Cr<sub>x</sub>-Nb-Ta (x = 5 or 20 at%) alloys, Table 5, indicating complex substitutional behaviour must occur. To understand the substitutional behaviour in the Laves phase in RHEAs, it is essential to review the chemical compositions of C15 observed in ternary systems. The C15 Laves phase with a chemical composition Ta(V, Cr)<sub>2</sub> was reported in the V-Cr-Ta ternary systems at 1200 °C [49], indicating V and Cr can substitute each other and occupy the B sites in the AB<sub>2</sub> structure. (Ti, Nb)Cr<sub>2</sub> and (Ta, Nb)Cr<sub>2</sub> were reported in the Ti-Cr-Nb and Cr-Nb-Ta ternary systems at 1300 °C and 1500 °C [50–52], indicating Ti, Nb and Ta preferentially occupy the A sites in C15 in the ternary systems. Based on these understandings, we may expect C15 in Ti-V-Cr-Nb-Ta with a composition of (Nb, Ti, Ta)(V, Cr)<sub>2</sub>. This is in agreement with the calculated composition of C15 phase, which predicts the equilibrium C15 phase contains ~55 at% Cr and ~10 at% V at 1200 °C. However, the stoichiometry of (Nb, Ti, Ta)(V, Cr)<sub>2</sub> is at substantial variance with elemental ratios measured by EDX, Table 5. Instead, [Ti, Ta] and [V, Cr, Nb] agrees with the AB<sub>2</sub> stoichiometry within the experimental error. It's well known that the atomic size rule and the electronic structure play important roles in the formation and stability of Laves phases [53]. Fig. 12 shows the Pauling electronegativity and atomic radius of five elements. V and Cr possess similar atomic size and Pauling electronegativity, and the same is true for Ti and Ta. Nb has similar atomic size as Ti and Ta but higher Pauling electronegativity. Therefore, from an electronic structure argument, Nb occupancy of V and Cr sites in C15 in RHEAs may also occur in the C15 phase under the experimental conditions. With

further annealing, Cr from the matrix may continue to diffuse to the Laves phase and substitute the previous Nb at B sites, which will lead to the C15 phase being close to the equilibrium composition of (Nb, Ti, Ta)(V, Cr)<sub>2</sub>. This implication will need more calculations and advanced microscopy analysis to confirm. In addition, from the isothermal section of the Ta-V-Cr ternary system [49], it can be seen that when Cr content is low, there is a small region in the isothermal section containing C14 Laves phase, which gives a direction for the further analysis of the unidentified nanoprecipitates in the 800 °C homogenised Ti-V-Cr5-Nb-Ta alloys as shown in Fig. 9(a).

## 6. Conclusions

Two refractory high entropy alloys, Ti-V-Cr5-Nb-Ta and Ti-V-Cr-Nb-Ta, were cast using vacuum arc melting and their crystal structures, chemical variation, microstructure and mechanical properties were determined in the as-cast and various homogenised conditions. The following conclusions were reached:

- Both alloys show almost single-phase BCC structure in their as-cast state, while different size and volume fraction of secondary phases were formed after homogenisation heat treatment. The Laves phase formed in both alloys is found a complex substitutional C15 structure.
- The nano-size precipitates formed in the 800 °C homogenised alloys are observed to cause local precipitate strengthening effects without significantly decreasing the ductility. The formation of micron-sized C15 Laves phase increases hardness, but acts as crack initiation sites during nanoindentation tests. This will likely result in significantly reduced ductility compared to the single phase variant.
- Based on experimental results, a two-step heat treatment process is proposed to introduce a fine second-phase dispersion in Ti-V-Cr5-Nb-Ta. First, annealing at high temperature (1200 °C) to achieve a fully-homogeneous single-phase microstructure, followed by a precipitation heat treatment at 800 °C to control the size and density of nano-precipitates.

## CRedit author contribution statement

**Junliang Liu:** Conceptualization, Methodology, Validation, Formal analysis, Data curation, Writing – original draft, Writing – review & editing, Visualization. **Robert J. Scales:** Methodology, Validation, Formal analysis, Visualization, Writing – review & editing. **Bo-Shiuan Li:** Methodology, Investigation, Formal analysis, Writing – review & editing. **Michael Goode:** Methodology, Investigation, Formal analysis, Visualization, Writing – review & editing. **Bradley A. Young:** Methodology, Investigation, Formal analysis, Writing – review & editing. **Jianan Hu:** Software, Formal analysis, Writing – review & editing. **Angus J. Wilkinson:** Conceptualization, Validation, Writing – review & editing, Supervision, Project administration, Funding acquisition. **David E. J. Armstrong:** Conceptualization, Validation, Resources, Writing – review & editing, Supervision, Project administration, Funding acquisition.

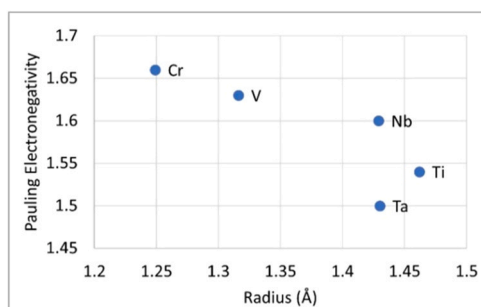


**Fig. 12.** Pauling electronegativity and atomic radius of elements in current study. The data were replotted using data from [47].

## Data Availability

Data will be made available on request.

## Declaration of Competing Interest

The authors declare that they have no known competing financial interests or personal relationships that could have appeared to influence the work reported in this paper.

## Acknowledgement

JL, BSL, AJW and DEJA acknowledge funding from EPSRC Grants EP/R021775/1, EP/R006245/1 and EP/P001645/1. EPSRC grant (EP/N010868/1) is acknowledged for funding the Zeiss Crossbeam FIB/SEM used in this research. The authors acknowledged the use of characterisation facilities within the David Cockayne Centre for Electron Microscopy, Department of Materials, University of Oxford.

## References

- [1] O.N. Senkov, D.B. Miracle, K.J. Chaput, J.-P. Couzinie, Development and exploration of refractory high entropy alloys—A review, *J. Mater. Res.* 33 (2018) 3092–3128, <https://doi.org/10.1557/jmr.2018.153>
- [2] C. Lee, G. Song, M.C. Gao, R. Feng, P. Chen, J. Brechtel, Y. Chen, K. An, W. Guo, J.D. Poplawsky, S. Li, A.T. Samaei, W. Chen, A. Hu, H. Choo, P.K. Liaw, Lattice distortion in a strong and ductile refractory high-entropy alloy, *Acta Mater.* 160 (2018) 158–172, <https://doi.org/10.1016/j.actamat.2018.08.053>
- [3] O.U. Tukac, A. Ozalp, E. Aydogan, Development and thermal stability of Cr10Mo25Ta25Ti15V25 refractory high entropy alloys, *J. Alloy. Compd.* 930 (2023) 167386, <https://doi.org/10.1016/j.jallcom.2022.167386>
- [4] A. Ayyagari, R. Salloom, S. Muskeri, S. Mukherjee, Low activation high entropy alloys for next generation nuclear applications, *Materialia* 4 (2018) 99–103, <https://doi.org/10.1016/j.mtl.2018.09.014>
- [5] A. Kareer, J.C. Waite, B. Li, A. Couet, D.E.J. Armstrong, A.J. Wilkinson, Short communication: 'Low activation, refractory, high entropy alloys for nuclear applications, *J. Nucl. Mater.* 526 (2019) 151744, <https://doi.org/10.1016/j.jnucmat.2019.151744>
- [6] J. Kitagawa, K. Hoshi, Y. Kawasaki, R. Koga, Y. Mizuguchi, T. Nishizaki, Superconductivity and hardness of the equiatomic high-entropy alloy HfMoNbTiZr, *J. Alloy. Compd.* 924 (2022) 166473, <https://doi.org/10.1016/j.jallcom.2022.166473>
- [7] Z. Cheng, J. Sun, X. Gao, Y. Wang, J. Cui, T. Wang, H. Chang, Irradiation effects in high-entropy alloys and their applications, *J. Alloy. Compd.* (2022) 166768, <https://doi.org/10.1016/j.jallcom.2022.166768>
- [8] W. Chen, Q.H. Tang, H. Wang, Y.C. Xie, X.H. Yan, P.Q. Dai, Microstructure and mechanical properties of a novel refractory AlNbTiZr high-entropy alloy, *Mater. Sci. Technol.* 34 (2018) 1309–1315, <https://doi.org/10.1080/02670836.2018.1446267>
- [9] F. Stein, A. Leineweber, Laves phases: a review of their functional and structural applications and an improved fundamental understanding of stability and properties, *J. Mater. Sci.* 56 (2021) 5321–5427, <https://doi.org/10.1007/s10853-020-05509-2>
- [10] L. Fang, J. Wang, X. Li, X. Tao, Y. Ouyang, Y. Du, Effect of Cr content on microstructure characteristics and mechanical properties of ZrNbTaHf0.2Crx refractory high entropy alloy, *J. Alloy. Compd.* 924 (2022) 166593, <https://doi.org/10.1016/j.jallcom.2022.166593>
- [11] C.M. Liu, H.M. Wang, S.Q. Zhang, H.B. Tang, A.L. Zhang, Microstructure and oxidation behavior of new refractory high entropy alloys, *J. Alloy. Compd.* 583 (2014) 162–169, <https://doi.org/10.1016/j.jallcom.2013.08.102>
- [12] N.N. Guo, L. Wang, L.S. Luo, X.Z. Li, Y.Q. Su, J.J. Guo, H.Z. Fu, Microstructure and mechanical properties of refractory MoNbHfZrTi high-entropy alloy, *Mater. Des.* 81 (2015) 87–94, <https://doi.org/10.1016/j.matdes.2015.05.019>
- [13] H. Chen, A. Kauffmann, B. Gorr, D. Schliephake, C. Seemüller, J.N. Wagner, H.J. Christ, M. Heilmaier, Microstructure and mechanical properties at elevated temperatures of a new Al-containing refractory high-entropy alloy Nb-Mo-Cr-Ti-Al, *J. Alloy. Compd.* 661 (2016) 206–215, <https://doi.org/10.1016/j.jallcom.2015.11.050>
- [14] D.B. Miracle, O.N. Senkov, A critical review of high entropy alloys and related concepts, *Acta Mater.* 122 (2017) 448–511, <https://doi.org/10.1016/j.actamat.2016.08.081>
- [15] S. Wei, S.J. Kim, J. Kang, Y. Zhang, Y. Zhang, T. Furuhashi, E.S. Park, C.C. Tassan, Natural-mixing guided design of refractory high-entropy alloys with as-cast tensile ductility, *Nat. Mater.* 19 (2020) 1175–1181, <https://doi.org/10.1038/s41563-020-0750-4>
- [16] F.G. Coury, T. Butler, K. Chaput, A. Saville, J. Copley, J. Foltz, P. Mason, K. Clarke, M. Kaufman, A. Clarke, Phase equilibria, mechanical properties and design of quaternary refractory high entropy alloys, *Mater. Des.* 155 (2018) 244–256, <https://doi.org/10.1016/j.matdes.2018.06.003>
- [17] O.N. Senkov, C.F. Woodward, Microstructure and properties of a refractory NbCrMo0.5Ta0.5TiZr alloy, *Mater. Sci. Eng. A* 529 (2011) 311–320, <https://doi.org/10.1016/j.msea.2011.09.033>
- [18] B. Kang, T. Kong, H.J. Ryu, S.H. Hong, Superior mechanical properties and strengthening mechanisms of lightweight AlxCrNbVMo refractory high-entropy alloys (x = 0, 0.5, 1.0) fabricated by the powder metallurgy process, *J. Mater. Sci. Technol.* 69 (2021) 32–41, <https://doi.org/10.1016/j.jmst.2020.07.012>
- [19] N.D. Stepanov, N.Y. Yurchenko, E.S. Panina, M.A. Tikhonovskiy, S.V. Zherebtsov, Precipitation-strengthened refractory Al0.5CrNbTi2V0.5 high entropy alloy, *Mater. Lett.* 188 (2017) 162–164, <https://doi.org/10.1016/j.matlet.2016.11.030>
- [20] E.J. Pickering, A.W. Carruthers, P.J. Barron, S.C. Middleburgh, D.E.J. Armstrong, A.S. Gandy, High-entropy alloys for advanced nuclear applications, *Entropy* 23 (2021), <https://doi.org/10.3390/e23010098>
- [21] G.R. Odette, M.J. Alinger, B.D. Wirth, Recent developments in irradiation-resistant steels, *Annu. Rev. Mater. Res.* 38 (2008) 471–503, <https://doi.org/10.1146/annurev.matsci.38.060407.130315>
- [22] Periodic Table | Creative Chemistry, (n.d.). <https://www.creative-chemistry.org.uk/gcse/periodic> (accessed December 14, 2021).
- [23] V.N. German, A.A. Bakanova, L.A. Tarasova, Y.N. Sutulov, Phase transformations in titanium and zirconium affected by shock waves, *Fizika Tverdogo Tela* 12 (1970) 637–639, <https://inis.iaea.org/search/search.aspx?orig.q=RN:1000202> (accessed January 7, 2022).
- [24] Y.A. Kocherzhinskii, V.V. Petkov, E.A. Shishkin, Phase equilibria and crystal structure of intermediate phases in the system tantalum-chromium, *Metallofizika* 46 (1973) 75–80.
- [25] G.M. Pharr, J.H. Strader, W.C. Oliver, Critical issues in making small-depth mechanical property measurements by nanoindentation with continuous stiffness measurement, *J. Mater. Res.* 24 (2009) 653–666, <https://doi.org/10.1557/JMR.2009.0096>
- [26] X. Li, B. Bhushan, A review of nanoindentation continuous stiffness measurement technique and its applications, *Mater. Charact.* 48 (2002) 11–36, [https://doi.org/10.1016/S1044-5803\(02\)00192-4](https://doi.org/10.1016/S1044-5803(02)00192-4)
- [27] P. Sudharshan Phani, W.C. Oliver, A critical assessment of the effect of indentation spacing on the measurement of hardness and modulus using instrumented indentation testing, *Mater. Des.* 164 (2019) 107563, <https://doi.org/10.1016/j.matdes.2018.107563>
- [28] W.C. Oliver, G.M. Pharr, An improved technique for determining hardness and elastic modulus using load and displacement sensing indentation experiments, *Journal of Materials Research* 7 (1992) 1564–1583, <https://doi.org/DOI:10.1557/JMR.1992.1564>
- [29] C.M. Magazzeni, H.M. Gardner, I. Howe, P. Gojon, J.C. Waite, D. Rugg, D.E.J. Armstrong, A.J. Wilkinson, Nanoindentation in multi-modal map combinations: a correlative approach to local mechanical property assessment, *J. Mater. Res.* 36 (2021) 2235–2250, <https://doi.org/10.1557/s43578-020-00035-y>
- [30] R. Castaing, Electron Probe Microanalysis, *Advances in Electronics and Electron Physics* 13 (1960) 317–386, [https://doi.org/10.1016/S0065-2539\(08\)60212-7](https://doi.org/10.1016/S0065-2539(08)60212-7)
- [31] Robert J. Scales, Macro-mechanical testing of novel high-entropy alloys for nuclear application, *Univ. Oxf.* (2020).
- [32] A. Leo, C. Hansch, D. Elkins, Partition coefficients and their uses, *Chem. Rev.* 71 (1971) 525–616, <https://doi.org/10.1021/cr60274a001>
- [33] B. Zhang, M.C. Gao, Y. Zhang, S.M. Guo, Senary refractory high-entropy alloy CrxMoNbTaVW, *Calphad* 51 (2015) 193–201, <https://doi.org/10.1016/j.calphad.2015.09.007>
- [34] H.W. Yao, J.W. Qiao, M.C. Gao, J.A. Hawk, S.G. Ma, H.F. Zhou, Y. Zhang, NbTaV(Ti,W) refractory high-entropy alloys: experiments and modeling, *Mater. Sci. Eng.: A* 674 (2016) 203–211, <https://doi.org/10.1016/j.msea.2016.07.102>
- [35] O.N. Senkov, G.B. Wilks, D.B. Miracle, C.P. Chuang, P.K. Liaw, Refractory high-entropy alloys, *Intermetallics* 18 (2010) 1758–1765, <https://doi.org/10.1016/j.intermet.2010.05.014>
- [36] M.G. Poletti, G. Fiore, B.A. Szost, L. Battezzati, Search for high entropy alloys in the X-NbTaTiZr systems (X = Al, Cr, V, Sn), *J. Alloy. Compd.* 620 (2015) 283–288, <https://doi.org/10.1016/j.jallcom.2014.09.145>
- [37] J.P. Couzinié, G. Dirras, L. Perrière, T. Chauveau, E. Leroy, Y. Champion, I. Guillot, Microstructure of a near-equimolar refractory high-entropy alloy, *Mater. Lett.* 126 (2014) 285–287, <https://doi.org/10.1016/j.matlet.2014.04.062>
- [38] J.J. Roa, G. Fargas, A. Mateo, E. Jiménez-Piqué, Dependence of nanoindentation hardness with crystallographic orientation of austenite grains in metastable stainless steels, *Mater. Sci. Eng.: A* 645 (2015) 188–195, <https://doi.org/10.1016/j.msea.2015.07.096>
- [39] X. Liu, R. Wang, A. Ren, J. Jiang, C. Xu, P. Huang, W. Qian, Y. Wu, C. Zhang, Evaluation of radiation hardening in ion-irradiated Fe based alloys by nanoindentation, *J. Nucl. Mater.* 444 (2014) 1–6, <https://doi.org/10.1016/j.jnucmat.2013.09.026>
- [40] H.H. Fu, D.J. Benson, M.A. Meyers, Analytical and computational description of effect of grain size on yield stress of metals, *Acta Mater.* 49 (2001) 2567–2582, [https://doi.org/10.1016/S1359-6454\(01\)00062-3](https://doi.org/10.1016/S1359-6454(01)00062-3)
- [41] Q. He, Y. Yang, On lattice distortion in high entropy alloys, *Front. Mater.* 5 (2018) <https://www.frontiersin.org/article/10.3389/fmats.2018.00042>
- [42] H. Chen, A. Kauffmann, S. Laube, I.-C. Choi, R. Schwaiger, Y. Huang, K. Lichtenberg, F. Müller, B. Gorr, H.-J. Christ, M. Heilmaier, Contribution of lattice distortion to solid solution strengthening in a series of refractory high entropy alloys, *Metall. Mater. Trans. A* 49 (2018) 772–781, <https://doi.org/10.1007/s11661-017-4386-1>
- [43] F.G. Coury, M. Kaufman, A.J. Clarke, Solid-solution strengthening in refractory high entropy alloys, *Acta Mater.* 175 (2019) 66–81, <https://doi.org/10.1016/j.actamat.2019.06.006>

- [44] E.J. Pickering, N.G. Jones, High-entropy alloys: a critical assessment of their founding principles and future prospects, *Int. Mater. Rev.* 61 (2016) 183–202, <https://doi.org/10.1080/09506608.2016.1180020>
- [45] S.I. Rao, C. Varvenne, C. Woodward, T.A. Parthasarathy, D. Miracle, O.N. Senkov, W.A. Curtin, Atomistic simulations of dislocations in a model BCC multi-component concentrated solid solution alloy, *Acta Mater.* 125 (2017) 311–320, <https://doi.org/10.1016/j.actamat.2016.12.011>
- [46] Y. Zhang, Y.J. Zhou, J.P. Lin, G.L. Chen, P.K. Liaw, Solid-solution phase formation rules for multi-component alloys, *Adv. Eng. Mater.* 10 (2008) 534–538, <https://doi.org/10.1002/adem.200700240>
- [47] S. Guo, C.T. Liu, Phase stability in high entropy alloys: formation of solid-solution phase or amorphous phase, *Prog. Nat. Sci. Mater. Int.* 21 (2011) 433–446, [https://doi.org/10.1016/S1002-0071\(12\)60080-X](https://doi.org/10.1016/S1002-0071(12)60080-X)
- [48] Z.-X. Xia, C.-Y. Wang, Y.-F. Zhao, G.-D. Zhang, L. Zhang, X.-M. Meng, Laves phase formation and its effect on mechanical properties in P91 steel, *Acta Metall. Sin.* 28 (2015) 1238–1246, <https://doi.org/10.1007/s40195-015-0318-5>
- [49] X.J. Liu, P. Yang, S.Y. Yang, J.J. Han, Y. Lu, Y.X. Huang, J.B. Zhang, C.P. Wang, Experimental investigations of phase equilibria in the Ta-V-Cr Ternary System, *J. Ph. Equilib. Diffus.* 41 (2020) 891–899, <https://doi.org/10.1007/s11669-020-00853-x>
- [50] J.C.J. Gigolotti, A.A.A.P. da Silva, G.C. Coelho, C.A. Nunes, J.-M. Joubert, Experimental study of the Cr-Hf-Nb system: liquidus projection and 1200 °C isothermal section, *J. Ph. Equilib. Diffus.* 41 (2020) 702–721, <https://doi.org/10.1007/s11669-020-00838-w>
- [51] L. Kaufman, H. Nesor, Calculation of superalloy phase diagrams: part III, *Metall. Trans. A* 6 (1975) 2115–2122, <https://doi.org/10.1007/BF03161838>
- [52] M.S. of A.I. of M.D.R.M. Committee, M. American Institute of Mining and Petroleum Engineers. Detroit Section, Refractory Metals and Alloys: Proceedings of a Technical Conference, Interscience Publishers, 1961. <https://books.google.co.uk/books?id=5IGHAFXJ-osC>
- [53] F. Chu, D.J. Thoma, P.G. Kotula, S. Gerstl, T.E. Mitchell, I.M. Anderson, J. Bentley, Phase stability and defect structure of the C15 laves phase Nb(Cr,V)<sub>2</sub>, *Acta Mater.* 46 (1998) 1759–1769, [https://doi.org/10.1016/S1359-6454\(97\)00291-7](https://doi.org/10.1016/S1359-6454(97)00291-7)